lubricants

MDPI

Article

Exposure-History-Dependent Hydrogen Retention and Release in 100Cr6 Steel and Their Implications for Bearing Design

He Liu [1,2,*], Sijie Yuan [1], Zhihao Wu [1], Jingwen Fang [3], Wanjia Li [4], Bochuan Li [5,6] and Wenhu Zhang [1]

[1] School of Mechatronics Engineering, Henan University of Science and Technology, Luoyang 471003, China
[2] Luoyang Bearing Research Institute Co., Ltd., Luoyang 471039, China
[3] Luoyang Bearing Group Co., Ltd., Luoyang 471039, China
[4] Zhengzhou Advanced Research Institute, Harbin Institute of Technology, Zhengzhou 450000, China
[5] State Key Laboratory of Advanced Design and Manufacturing for Vehicle Body, College of Mechanical and Vehicle Engineering, Hunan University, Changsha 410082, China
[6] Greater Bay Area Institute for Innovation, Hunan University, Guangzhou 511300, China
* Correspondence: liu.he@haust.edu.cn

Abstract

This study examines operational hydrogen memory in hardened 100Cr6 bearing steel using an analytical model constrained by published room-temperature effusion and FE8 accumulation measurements. The primary single-exponential retention model has an apparent room-temperature half-life of 63.4 h; an added fast decay was poorly identifiable. An effective input inferred from the 30 h FE8 measurement reproduced the 50 h increment within 0.3% as a conditional source-scale check. For 10 h of input at 0.005 ppm per hour followed by a 40 h interruption, the first interruption removed 35.4% of the releasable hydrogen. The post-interruption residual increased from 0.0306 ppm after the first cycle to 0.0725 ppm after 12 cycles, approaching a periodic value of 0.0726 ppm. When cumulative input and interruption times were both fixed at 120 h, replacing one long input–interruption pair with 24 shorter pairs increased the final releasable hydrogen content from 0.0899 to 0.2062 ppm. The exposure sequence thus determines the residual state alongside cumulative durations. This ordering persisted in conditional bootstrap and leave-one-out calculations and the exploratory two-exponential comparison. The results support comparing both peak content and the residual before renewed loading, using measured uptake and release responses to screen effective entry and sustained low-input interruptions for candidate bearing designs.

Keywords: rolling bearings; hydrogen retention; hydrogen trapping; intermittent hydrogen exposure; operating history; bearing design

Check for updates

Received: 14 September 2026
Revised: 16 October 2026
Accepted: 16 October 2026
Published: 18 October 2026

Copyright: © 2026 by the authors. Licensee MDPI, Basel, Switzerland. This article is an open access article distributed under the terms and conditions of the Creative Commons Attribution (CC BY) license.

1. Introduction

Hydrogen in rolling-bearing steel can substantially alter its damage response and contribute to premature bearing damage. Early four-ball tests on hydrogen-impregnated AISI 52100 showed that rolling-contact fatigue life decreased with increasing hydrogen content [1]. Brittle flaking, white etching areas (WEAs), and white etching cracks (WECs) were subsequently reproduced under hydrogen-containing conditions [2–5]. WEAs are altered microstructural regions, whereas WECs are cracks associated with such regions [4,5]. More recent rolling-contact and rolling/sliding tests also found higher void and crack densities and larger damaged-area fractions in hydrogen-containing 100Cr6 [6,7]. Weniger et al. [6] used NaOH electrolyte with thiourea for charging, whereas Liang et al. [7] used

NaCl solution at 80 °C. Hydrogen charging affects WEC initiation and development under rolling contact [8,9]. Proposed formation routes involve local stress, inclusions and microstructural evolution [10]. Reviews also identify sliding, electrical effects and lubricant chemistry as contributing factors [11,12]. For bearings operated under variable conditions, hydrogen generated during one period of contact can remain in the steel during an interruption and be carried into the next loading period. Evaluating this inherited state requires consideration of both entry during operation and release between exposures.

Hydrogen available during bearing operation can originate from moisture, corrosion reactions, gaseous hydrogen exposure, and decomposition of hydrogen-containing lubricants on wear-induced nascent steel surfaces [2,13–15]. Lubricant decomposition is particularly relevant to lubricated rolling contacts because sliding, surface renewal, tribofilm formation, and lubricant chemistry affect the local supply. Hydrogen-containing reaction products were detected during lubricant degradation in in situ mass-spectrometric sliding experiments [14], while bearing tests linked lubricant formulation to post-test hydrogen content and WEA/WEC-type damage [13,15,16]. The FE8 measurements further show how hydrogen content changes with operating duration. Richardson et al. reported increasing hydrogen content in 100Cr6 rolling elements but little measurable hydrogen in the corresponding raceways [17]. In the FE8 washers investigated by Linzmayer et al., freely movable hydrogen increased from 0.055 ppm in the reference material to 0.159 ppm after 30 h and 0.212 ppm after 50 h; diffusible hydrogen increased from 0.873 to 1.032 ppm after 30 h [18]. These net changes in washer or rolling-element hydrogen content reflect the combined effects of generation, entry, transport, trapping, redistribution, and release during operation.

Hydrogen is one contributor within this coupled damage process. Linzmayer et al. [18] also note that WEC has been reported with hydrogen-free lubricants. A PFPE base fluid lacks hydrogen in its molecular backbone, but its use alone does not establish the absence of other hydrogen sources in a complete bearing system. Kürten et al. [15] observed no hydrogen-induced damage with the tested PFPE under their conditions. Peripheral components can also change WEC behavior: Wranik et al. [19] obtained WECs with polyamide hoses but no failure with silicone or stainless steel hoses using the same low-reference oil. Lubricant formulation and the surrounding system therefore need to be specified when interpreting damage and hydrogen supply.

Once hydrogen enters bearing steel, microstructural trapping strongly affects its mobility and retention. The McNabb–Foster and Oriani descriptions established the kinetic and equilibrium foundations for interactions between mobile and trapped hydrogen [20,21], and later studies classified hydrogen traps and quantified their effects on apparent solubility and diffusivity [22–27]. Candidate trapping features in bearing steel include dislocations, grain boundaries, carbide/matrix interfaces, retained austenite, inclusions, and deformation-generated defects [28–32]. Baur et al. resolved several hydrogen desorption peaks in 100Cr6 and measured a decrease in total hydrogen content from approximately 3 ppm to approximately 1.8 ppm during 400 h of room-temperature effusion from gas-charged hardened 100Cr6 [29]. This prolonged release makes both the interruption duration and the remaining hydrogen content relevant to start–stop bearing operation. History-dependent responses during repeated charging, release, and recharging have also been reported for other steels [33,34]. Bearing investigations have commonly evaluated hydrogen after a continuous test or a single charging–effusion sequence [4,5,7,17,18,29,35]. Repeated exposure therefore calls for a quantitative description of how input and interruption durations, together with their sequence, determine the hydrogen retained before renewed loading.

Successive rolling elements impose contact pulses at a material point on the raceway. Rolling-element number, pitch diameter, rolling-element diameter, contact angle and rela-

tive rotational speeds affect their recurrence, while contact size also affects their duration. Raceway dimensions and curvatures influence contact geometry; ring wall thickness, axial width and support stiffness influence deformation and load distribution. Applied load, clearance and preload determine the extent of load sharing [36]. These geometrical and operating variables can therefore alter the duration, spacing and severity of contact without a shaft stop. Different histories at the inner and outer raceways provide one example of why the resulting exposure sequence should be evaluated for the intended bearing design and operating conditions.

This study aims to clarify how the timing of intermittent hydrogen supply controls releasable hydrogen content in 100Cr6 bearing steel and to examine its implications for bearing design. The residual state inherited from earlier exposure is termed operational hydrogen memory in this study. We used published room-temperature effusion data to determine a primary single-exponential retention model and benchmarked an effective hydrogen input scale against published FE8 accumulation measurements, accounting for release during exposure. The analytical ON–OFF relations were then used to calculate cyclic states, compare histories with equal cumulative exposure, and determine reset times. An independently refitted two-component form is retained for exploratory model comparison. Model-form comparisons, conditional bootstrap refits and leave-one-out calculations assess the consistency of the exposure history effect. We discuss the bearing-design implications by relating geometry, contact and lubrication conditions, and material retention to hydrogen input and release before renewed loading.

2. Numerical Model and Methodology

2.1. Modeling Concept and Scope

Temporal retention of releasable hydrogen is described by a reduced-order model with one apparent room-temperature release timescale in the primary calculations constrained by published total-effusion measurements. Spatial hydrogen diffusion is not calculated. The general fast- and slow-release components are denoted $C_f(t)$ and $C_s(t)$, respectively; the primary single-exponential model sets the fast component to zero. The component labels are empirical and do not identify specific microstructural traps. This distinction is necessary because thermal desorption mass spectrometry (TDMS) peak activation energies cannot be interpreted directly as microscopic detrapping constants without a dedicated reaction–diffusion analysis.

Figure 1 shows the engineering setting and its analytical representation. Figure 1a illustrates intermittent hydrogen entry at a lubricated rolling-bearing contact. In Figure 1b, the effective hydrogen input rate, q_c, supplies each active release component during the ON period, while release proceeds during both ON and OFF periods. If an OFF period is insufficient for complete release, the next ON period begins with non-zero residual hydrogen content. This inherited state is the subject of the temporal calculation. Here, ON denotes sustained effective hydrogen supply, and OFF denotes an interval with negligible effective input. These definitions specify the source conditions used in the calculation.

Equation (1) defines the total releasable hydrogen content as the sum of the fast- and slow-release components:

$$C_R(t) = C_f(t) + C_s(t) \quad (1)$$

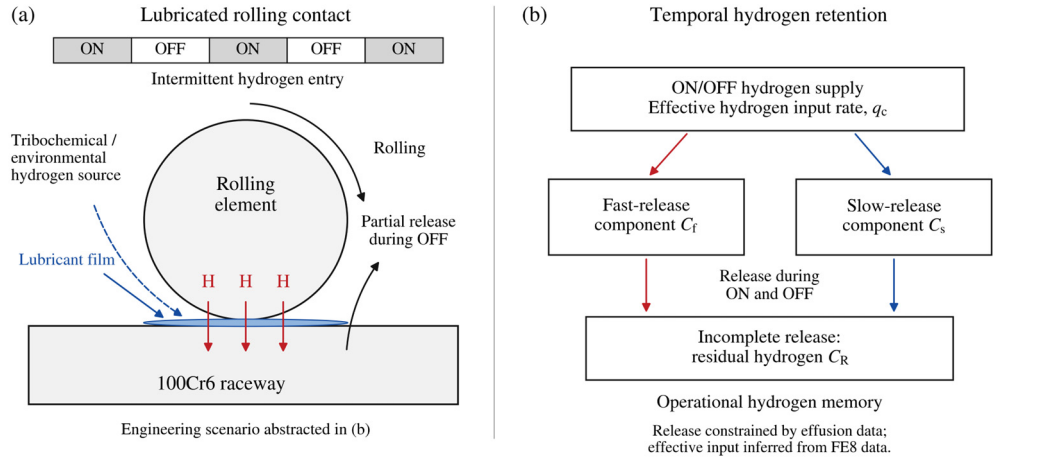


Figure 1. Engineering context and reduced-order analytical model: (**a**) schematic lubricated rolling contact with intermittent near-surface hydrogen entry during ON periods and partial release during OFF periods; (**b**) reduced-order framework linking the effective hydrogen input rate to the general apparent fast- and slow-release components and the residual state associated with operational hydrogen memory. The primary model uses the one-active-component limit, with zero fast amplitude and source fraction; the two-component drawing does not identify two physical trap populations. The ON and OFF intervals represent effective hydrogen supply and interruption; their durations are not calibrated to individual rolling-element passages.

2.2. Room-Temperature Hydrogen Retention Model from Published 100Cr6 Effusion Data

The temporal retention model was constrained using the room-temperature effusion measurements of Baur et al. [29]. Hardened 100Cr6 bearing elements were charged to approximately 3 ppm hydrogen, after which total hydrogen content was measured at different effusion durations up to 400 h. Because the raw numerical data were not published, ten mean points were digitized from Figure 7 of Ref. [29]. These digitized literature data constrain the temporal response of the reduced-order model.

For the measured total hydrogen content, Equation (2) combines two empirical release components with a constant background term in the general hydrogen retention framework; the primary single-exponential case sets the fast amplitude to zero:

$$C_{tot}(t) = C_\infty + A_f \exp(-k_f t) + A_s \exp(-k_s t) \quad (2)$$

where C_∞ denotes the constant background term over the 400 h observation window. The amplitudes A_f and A_s correspond to the fast- and slow-release components, whose apparent release rate constants are k_f and k_s, respectively. The background term C_∞ accounts for the long-time offset required to fit the available 400 h dataset; it does not denote an irreversible trap capacity.

The measured total content is $C_{tot}(t)$, whereas $C_R(t)$ in Equation (1) is its fitted decaying contribution after subtracting the constant background. Both are expressed in mass ppm. The primary model sets $A_f = 0$, $A_s = A$ and $k_s = k$; its reference in Equation (3) is therefore $C_{R,ref} = A$. Equation (4) is evaluated only for an active component. Terms for the inactive component are omitted from evaluation.

$$C_{R,ref} = A_f + A_s \quad (3)$$

Table 1 lists the primary single-exponential parameters for the digitized effusion dataset. The corresponding half-lives are calculated from Equation (4).

Table 1. Primary single-exponential room-temperature retention parameters for hardened 100Cr6, expressed in the general two-component notation.

Quantity	Value	Role in Present Model	Source/Status
Constant background term over 400 h	1.82503 ppm	Offset of total-effusion fit; excluded from dynamic releasable hydrogen content	Reference parameterization of mean values digitized from Figure 7 of Baur et al. [29]
Fast-release amplitude	0 ppm	Inactive in primary model	Same reference parameterization
Fast apparent release rate constant	Not active	Not used in primary calculations	Same reference parameterization
Fast apparent half-life	Not active	Not used in primary calculations	Zero fast amplitude
Slow-release amplitude	1.08259 ppm	Single active decaying amplitude	Same reference parameterization
Slow apparent release rate constant	0.0109399 h^{-1}	Dynamic release rate	Same reference parameterization
Slow apparent half-life	63.36 h	Derived timescale	Calculated from reference rate
Reference releasable hydrogen content	1.08259 ppm	Normalization reference; not trap capacity	Sum of reference releasable amplitudes
TDMS activation-energy range	Approx. 30–48 kJ/mol	Supports multiple hydrogen states; not used as kinetic rate constants	Baur et al. [29]

The three-parameter single-exponential primary model contains one decaying amplitude and a constant offset: 1.82503 ppm, 1.08259 ppm and 0.0109399 per hour for the offset, amplitude and apparent release rate constant, respectively. The revised supplementary analysis separately refits both forms to the ten archived means by unweighted nonlinear least squares, using nonnegative offsets and amplitudes, positive rate constants and multiple starting values. The solver settings and full precision refit results are supplied with the code. All main operating history analyses use the single-exponential parameters in Table 1. The independently refitted two-component form is retained only as an exploratory comparison.

We compared the model forms using the root-mean-square error (RMSE), coefficient of determination and corrected Akaike information criterion (AICc) under independent Gaussian residuals with a common estimated variance. The AICc parameter count includes this variance, giving four estimated parameters for the single-exponential model and six for the two-timescale model at $n = 10$. The same additive Gaussian constant is omitted from both scores. Section 3.1 reports refit diagnostics and model form comparisons; Section 2.7.5 compares the operating history outputs.

$$t_{1/2,j} = \frac{\ln 2}{k_j}, \qquad j \in \{\mathrm{f}, \mathrm{s}\} \tag{4}$$

2.3. Conditional Effective Hydrogen Input Benchmarks from FE8 Measurements

For continuous ON exposure from zero additional releasable hydrogen content, Equation (5) gives the increase in component j (f or s; only s is active in the primary model) while accounting for release during hydrogen input:

$$C_j(t) = \frac{w_j q_c}{k_j}\left[1 - \exp\left(-k_j t\right)\right] \tag{5}$$

where w_j denotes the fraction of the effective source allocated to release component j. Equation (6) determines the amplitude-based source partition from the fitted fast- and slow-release amplitudes:

$$w_f = \frac{A_f}{A_f + A_s}, \qquad w_s = \frac{A_s}{A_f + A_s} \tag{6}$$

For the primary single-exponential case, the amplitude-based partition gives $w_f = 0$ and $w_s = 1$. Since the published FE8 values represent net concentration increases, they cannot be used directly as q_c. The effective hydrogen input rate is obtained by inverting the accumulation relation in Equation (7):

In Equation (7), $\Delta C_{obs} = H(t_{obs}) - H_0$ is the measured net hydrogen increase in mass ppm, H_0 is the corresponding untested material reference, and t_{obs} is the test duration in hours. The source q_c is an equivalent input per unit steel mass in ppm/h; it is not a measured interfacial hydrogen flux.

$$q_c = \frac{\Delta C_{obs}}{\sum_{j\in\{f,s\}} \frac{w_j}{k_j}\left[1 - \exp\left(-k_j t_{obs}\right)\right]} \tag{7}$$

Table 2 lists the conditional effective hydrogen input benchmarks calculated from the published net increases using Equation (7).

Table 2. Measurement-specific FE8 observations and conditional effective hydrogen input benchmarks.

Literature Observation	Net Increase	Duration	Conditional Hydrogen Input Benchmark	Use in This Study
FE8 washer, freely movable H; HCA at 210 °C [18]	0.104 ppm	30 h	0.0040666 ppm/h	Primary conditional source scale
FE8 washer, freely movable H; HCA at 210 °C [18]	0.157 ppm	50 h	0.0040767 ppm/h	Second-time source-scale comparison
FE8 washer, diffusible H; HCA at 400 °C [18]	0.159 ppm	30 h	0.0062172 ppm/h	Assay-dependent sensitivity scale
FE8 rolling-element H; ramped TDA–GC [17]	approx. 0.38 ppm	approx. 18 h	approx. 0.02326 ppm/h	Upper illustrative source scale

Linzmayer et al. [18] tested 81212 thrust bearings at 80 kN, 300 rpm, a bearing temperature of 100 °C and an oil flow of 0.25 L/min. Their freely movable hydrogen category was measured by hydrogen collection analysis (HCA), using 24 h collection at 210 °C followed by thermal conductivity detection. HCA at 400 °C includes this freely movable fraction and hydrogen associated with reversible shallow traps; room-temperature local hydrogen analysis is a separate electrochemical method. Richardson et al. [17] tested at 60 kN, 750 rpm and 100 °C; the rolling-element values used here were measured by ramped thermal desorption with gas chromatographic analysis (setup 2 in ref. [17]).

The FE8 temperature differs from that of the room-temperature release data. Equation (7) therefore provides a conditional source-amplitude scale under the selected kernel rather than a temperature-consistent calibration of uptake and release.

The effective hydrogen input rate inferred from the 30 h freely movable hydrogen increase was used to calculate the 50 h increase without refitting, as a conditional source-scale consistency check within the same experimental series. Other hydrogen metrics differ in measurement definition and specimen location and were retained as additional assay-dependent source scales. The regime map covers $0.004 \leq q_c \leq 0.024$ ppm/h, with $q_c = 0.005$ ppm/h selected as the representative baseline.

For the primary HCA series, the published reference, 30 h and 50 h contents are 0.055 ± 0.003, 0.159 ± 0.028 and 0.212 ± 0.054 ppm [18]. The source describes the displayed scatter as empirical variance incorporating within-washer and between-washer variation. We retain the displayed extents as deterministic sensitivity bounds, without assigning an unsupported standard deviation or confidence interpretation. Their joint propagation with a shared reference is specified in Section 2.7.4.

2.4. Intermittent ON–OFF Retention Model

During an ON period, Equation (8) balances effective hydrogen input and release for component j:

$$\frac{dC_j}{dt} = w_j q_c - k_j C_j \tag{8}$$

With the hydrogen input removed during an OFF period, each component releases hydrogen according to Equation (9):

$$\frac{dC_j}{dt} = -k_j C_j \tag{9}$$

Equation (10) gives the exact ON-period update over a duration Δt, including both the inherited hydrogen content and the effective input:

$$C_j(t + \Delta t) = C_j(t)\exp(-k_j \Delta t) + \frac{w_j q_c}{k_j}\left[1 - \exp(-k_j \Delta t)\right] \tag{10}$$

For the same inherited state with the input removed, Equation (11) gives the exact OFF-period update:

$$C_j(t + \Delta t) = C_j(t)\exp(-k_j \Delta t) \tag{11}$$

The closed-form ON- and OFF-period updates in Equations (10) and (11) are evaluated directly for each cycle. Because the model is linear, these exact updates introduce no time discretization error into the cycle calculations.

Here, C_j is the releasable content of component j in mass ppm, k_j is its apparent release rate in h^{-1}, Δt is the interval duration in hours, and w_j is its dimensionless source fraction. The initial content in an update is the state inherited from the preceding interval. For the primary model, $w_f = 0$ and $w_s = 1$; all input and residual content belong to the single active component.

2.5. Reference Operating Cycle and Parameter Settings

The reference cycle consists of $t_{on} = 10$ h of hydrogen input followed by $t_{off} = 40$ h of interruption. These durations were selected to represent intermittent exposure and are not assigned to a specific bearing duty cycle. Table 3 summarizes the operating conditions and parameter ranges; the retention parameters are listed in Table 1.

Table 3. Operating conditions and parameter ranges.

Input/Definition	Baseline or Range	Provenance	Interpretation
Baseline effective hydrogen input rate	0.005 ppm/h	Within conditional FE8 source scales	Representative source level
Effective hydrogen input rate range	0.004–0.024 ppm/h	Conditional inversion of [17,18] under the selected release kernel	Illustrative source-scale sensitivity range
ON duration	10 h	Present study choice	Reference intermittent sequence
OFF duration	40 h	Present study choice	Reference intermittent sequence
Reset criteria	0.10, 0.05, 0.02	Present study numerical definitions	Not hydrogen-damage thresholds
Baseline source partition	0 fast/1 slow	Single active component	Primary single-exponential case

2.6. Periodic Residual Hydrogen Content, Memory Index, and Reset Time

Equation (12) gives the steady pre-ON hydrogen content of component j after repeated application of the ON–OFF sequence:

Here, ss denotes the periodic steady state, and pre denotes the end of OFF, immediately before the next ON interval. $C_{j,\mathrm{ss}}^{\mathrm{pre}}$ is the residual of component j at this phase, and $C_{\mathrm{res,ss}}$ in Equation (13) is the sum over active components.

$$C_{j,\mathrm{ss}}^{\mathrm{pre}} = \frac{\exp\left(-k_j t_{\mathrm{off}}\right) \frac{w_j q_c}{k_j} \left[1 - \exp\left(-k_j t_{\mathrm{on}}\right)\right]}{1 - \exp\left[-k_j \left(t_{\mathrm{on}} + t_{\mathrm{off}}\right)\right]} \tag{12}$$

Summing the active steady pre-ON components gives the total periodic steady-state residual hydrogen content in Equation (13):

$$C_{\mathrm{res,ss}} = \sum_{j \in \{\mathrm{f,s}\}} C_{j,\mathrm{ss}}^{\mathrm{pre}} \tag{13}$$

Equation (14) defines the normalized hydrogen memory index used in this study by dividing the periodic residual by the reference releasable hydrogen content:

$$M_{\mathrm{H}} = \frac{C_{\mathrm{res,ss}}}{C_{\mathrm{R,ref}}} \tag{14}$$

The dimensionless persistence index is normalized by the fitted releasable hydrogen content. It may exceed unity outside the calibration-scale operating window because the denominator is a reference value from the fit, not the maximum trap capacity of the material. Its value does not denote a trap capacity fraction.

For a specified normalized residual criterion ε, Equation (15) defines the hydrogen reset time as the minimum interruption duration that satisfies the criterion:

$$t_{\mathrm{reset}}(\varepsilon) = \min\{t_{\mathrm{off}} : M_{\mathrm{H}} \leq \varepsilon\} \tag{15}$$

The criteria $\varepsilon = 0.10$, 0.05, and 0.02 were selected to describe different degrees of resetting relative to the fitted reference hydrogen content. They are numerical definitions rather than experimentally established embrittlement thresholds. Each reset time is the minimum OFF duration for the specified repeating cycle at a periodic steady state. Release during a single shutdown must instead be evaluated from the inherited state using Equation (11).

2.7. Analytical Implementation and Analysis Procedures

Table 4 summarizes the analytical evaluation procedure. We evaluated cycle histories with Equations (10) and (11), and periodic states and reset times with Equations (12)–(15). The implementation uses Python 3.12.14, with NumPy 2.3.5 and pandas 2.2.3 for numerical data handling and SciPy 1.17.0 for the independent refits. The supporting data and Python code are provided in the Supplementary Materials.

Table 4. Analytical evaluation procedure for operational hydrogen memory.

Step	Procedure
1	Read the literature-derived release parameters, source-partition coefficients, effective hydrogen input rate, ON duration, OFF duration, and requested cycle or parameter range.
2	Initialize the active releasable component to zero relative to the modeled reference state.
3	Apply the closed-form ON-period update in Equation (10) for the specified hydrogen-input duration.
4	Apply the closed-form OFF-period update in Equation (11) for the specified interruption duration, and use the resulting residual as the initial state of the next cycle.
5	Repeat the ON–OFF mapping for the prescribed number of cycles, or evaluate the periodic pre-input state directly from Equation (12).
6	Calculate the periodic residual, normalized hydrogen memory index, and reset time using Equations (13)–(15); repeat the analytical evaluation over the required parameter space when conducting sensitivity or operating history analyses. Propagate jointly refitted parameters and FE8 endpoint scenarios as specified in Section 2.7.4.

The exposure schedules, parameter ranges, and model variants used in the analyses are specified below in Sections 2.7.1–2.7.5.

2.7.1. Phase-Resolved Transient State Analysis

For the first 12 cycles, the total releasable hydrogen content was calculated directly from Equations (10) and (11) at common phase points covering each ON–OFF period. The values were organized into cycle-by-phase matrices to describe the approach to a periodic response. Within each cycle, the state was also separated into hydrogen inherited at its start and hydrogen introduced during its ON interval. The inherited contribution follows Equation (11) over the elapsed cycle time; the current-cycle contribution follows Equation (10) from zero during ON and Equation (11) during OFF. These are exposure-age contributions to the same single-rate state rather than separate trap populations. For each transient phase profile, its difference from the periodic profile was normalized by the difference at cycle start; the common phase dependence is $\exp(-k\tau)$.

2.7.2. Equal Cumulative Exposure History Analysis

The influence of the exposure sequence was examined by fixing the cumulative hydrogen-input duration and cumulative interruption duration at 120 h each and varying only the number of alternating ON–OFF segments. The schedules contain one, four, 12, or 24 segments. For a schedule with N segments, the input and interruption durations are each $120/N$ h per segment, with input first and interruption last. The effective hydrogen input rate and retention parameters were held constant for all schedules. Any difference

in the final state arises from temporal segmentation since the total hydrogen-input time, interruption time, elapsed time, and model parameters are identical.

2.7.3. Operating History Parameter Sweep

The analytical periodic state was evaluated over prescribed ranges of the operating history parameters. For the input rate/interruption map, the effective hydrogen input rate ranges from 0.004 to 0.024 ppm/h at 0.0001 ppm/h increments, and the interruption duration ranges from 5 to 250 h at 1 h increments, with the baseline input duration fixed at 10 h. For the duty history map, the input duration ranges from 1 to 60 h and the interruption duration from 5 to 200 h, both at 1 h increments, while the hydrogen input rate is fixed at 0.005 ppm/h. The periodic state for each combination is obtained from Equation (12), and the normalized hydrogen memory index and reset criteria are calculated from Equations (14) and (15). Each mapped point represents a directly evaluated periodic state rather than an interpolation of transient results.

2.7.4. Conditional Uncertainty and Observation Sensitivity Analysis

Parametric bootstrap calculations generated 500 single-exponential datasets at the original ten times using independent additive Gaussian residuals with the standard deviation $(\mathrm{SSE}/n)^{1/2}$ = 0.10317 ppm and random seed 20261014. Each full parameter vector was jointly refitted. Outputs were propagated separately at fixed q_c = 0.005 ppm/h and with q_c re-inverted from the unchanged 0.104 ppm, 30 h FE8 increment for every refit. Each refit uses its own amplitude as $C_{R,ref}$. The reported 2.5th–97.5th percentile ranges are conditional on this residual model; they are not experimental uncertainty intervals for graphical readings, hydrogen assays or bearing predictions. Ten leave-one-out fits provide a separate influence check.

The FE8 observation spreads were propagated separately by evaluating all eight lower/upper combinations of the reference, 30 h and 50 h contents listed in Section 2.3. The same reference value was used for both net increases within each scenario. No probability distribution was assigned to these endpoints, and their envelope was not combined with the bootstrap into an experimental confidence interval.

2.7.5. Model Form and Release Rate Robustness Assessment

Robustness was examined with respect to model form and release rates. The exploratory two-component model was independently refitted and evaluated at the same fixed hydrogen input rate and under the same schedules as the primary single-exponential model. Its amplitude-based source allocation in Equation (6) is an exploratory assumption. Rate profiles, fitted Jacobian rank and 200 two-component bootstrap refits were used to examine identifiability and fitting stability. The numerical rate domain was 10^{-6}–10^{3} h^{-1}, with the fast-rate profile additionally evaluated up to 10^{4} h^{-1}; these are solver domains rather than measured kinetic bounds. Separately, the primary single release rate was varied from 80% to 120% at 1% increments, while its amplitude and the effective input remained fixed. The normalized memory index, 10% periodic reset time and 24-segment/one-segment final-content ratio were recalculated.

A separate 90 °C comparison used 13 graphical release rate readings (ppmw/min) over 80–238 min for an uncracked 52100 plate (40 × 12 × 2 mm; 7 h charging) reported by Solano-Alvarez et al. [37]. Single- and double-exponential forms were fitted independently; fitting the first ten readings (80–195 min) and predicting the final three (210–238 min) supplied a chronological check. The graphical bounds were $\pm 6.369 \times 10^{-5}$ ppmw/min and ±0.324 min. The fitting and graphical sensitivity procedures are detailed in README.md in the Supplementary Materials. These separate rate fits do not calibrate or transfer the room-temperature inventory model.

3. Results

3.1. Literature-Based Retention Fit and Conditional Source-Scale Comparison

Figure 2a compares the single-exponential and two-timescale fits with the digitized room-temperature effusion measurements of Baur et al. [29]. The curves nearly overlap: the single-exponential reference gives an RMSE of 0.1032 ppm and R^2 of 0.9220, compared with 0.1022 ppm and 0.9235 for the two-timescale reference. Their residual patterns are also similar, as shown in Figure 2c. Independent multistart refits favor the single-exponential form, with nominal AICc values of −29.4 and −5.6 for the single- and two-timescale models, respectively. The two-timescale fit has the Jacobian rank four for five mean parameters, and its fast-rate profile is effectively flat above approximately 4 h^{-1}. The total-effusion data alone therefore do not statistically establish two distinct decay constants. The single-exponential fit is therefore used as the primary representation, with an apparent release half-life of 63.36 h. Figure 2b shows its fitted background and releasable term. Multiple TDMS peaks reported for 100Cr6 [29] do not by themselves identify two decay constants in the present total-effusion curve.

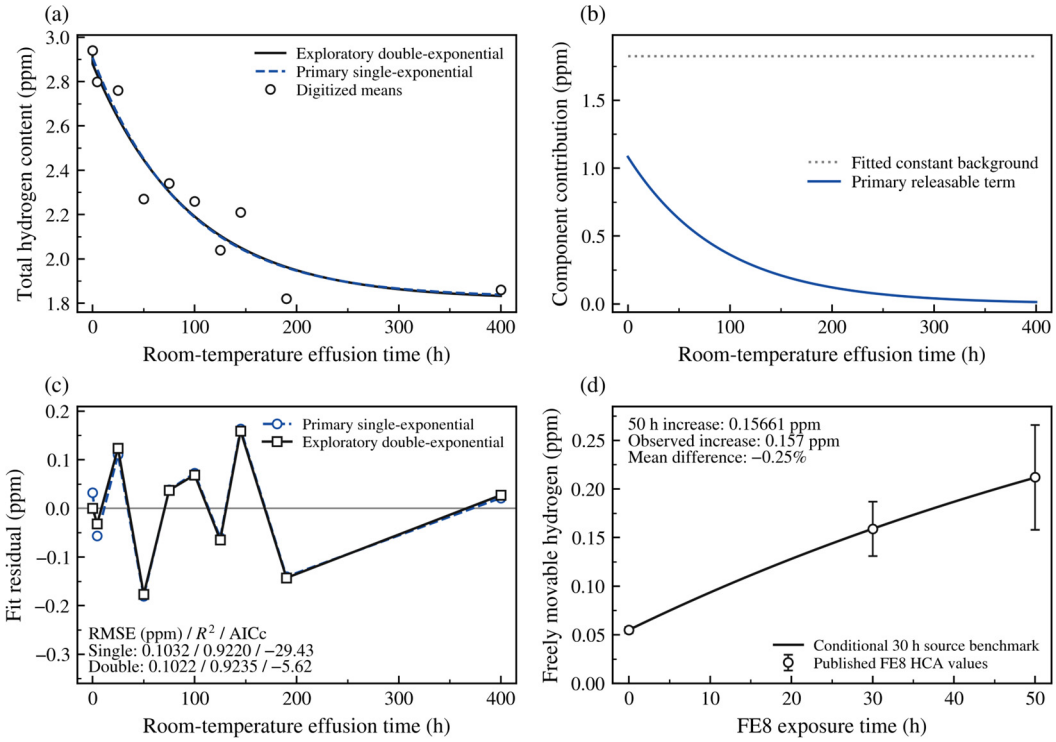


Figure 2. Literature-based model form comparison, primary parameterization, and conditional source-scale comparison: (**a**) single-exponential and exploratory two-timescale fits to mean room-temperature effusion values digitized from Figure 7 of Baur et al. [29]; (**b**) the fitted constant background and releasable term of the primary single-exponential representation; (**c**) residuals for both fits; and (**d**) FE8 freely movable hydrogen and the conditional source benchmark obtained from the 30 h increase. Error bars in (**d**) reproduce the reported scatter (0.003, 0.028 and 0.054 ppm), whose confidence level is unspecified; the 50 h increase is a second-time source-scale comparison.

Figure 2d shows the conditional source-scale comparison using the 50 h point from the same FE8 freely movable hydrogen series. Inversion of the 30 h increase gives an effective hydrogen input rate of 0.0040666 ppm/h, which gives a 50 h increase of 0.15661 ppm without refitting. The published increase is 0.157 ppm [18], and the relative difference is approximately −0.25%. This agreement is a source-scale consistency comparison within the same FE8 series under the assumed kernel. The FE8 bearing body temperature was 100 °C, so this calculation does not validate transfer of the room-temperature release rate. A

separate approximation of a published 90 °C release rate curve is provided in Figure S1 [37], with all parameters fitted independently.

3.2. Baseline Cyclic Evolution and Approach to the Periodic State

Figure 3a shows the cyclic evolution of releasable hydrogen content at the baseline input rate of 0.005 ppm/h, with shaded bands denoting the hydrogen-input periods. During the first 10 h input period, total releasable hydrogen content reaches 0.04736 ppm and then decreases to 0.03058 ppm over the subsequent 40 h interruption. The first interruption therefore removes approximately 0.01679 ppm, or 35.44%, of the releasable hydrogen present at the end of the preceding input period. The second cycle begins with hydrogen retained from the first. Over the 12 cycles, the progressive rise in the lower envelope reflects hydrogen carried from one cycle to the next. Release of this inherited inventory and new input are governed by the same primary rate constant.

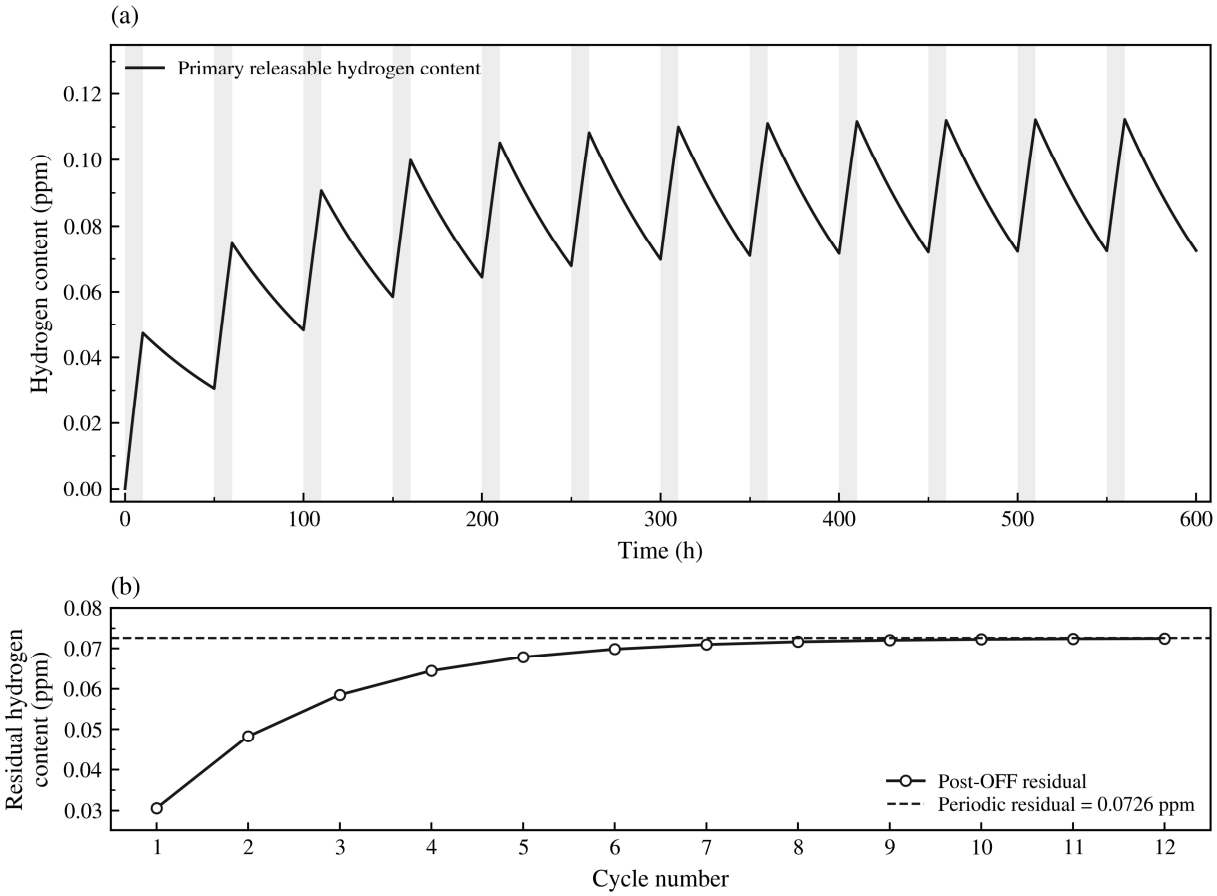


Figure 3. Baseline cyclic response under repeated intermittent hydrogen supply: (**a**) total releasable hydrogen content under the primary single-exponential model during 12 identical ON–OFF cycles; shaded regions denote hydrogen-input periods; (**b**) convergence of the post-interruption residual toward the analytical periodic state.

The post-interruption residual increases from 0.06444 ppm after four cycles to 0.07166 ppm after eight cycles and 0.07247 ppm after 12 cycles, approaching the analytical periodic value of 0.07257 ppm in Figure 3b. This value corresponds to a normalized hydrogen memory index of approximately 0.0670. Accumulation is limited because hydrogen continues to be released during both input and interruption. Under the repeated baseline schedule, the inherited state approaches a periodic dynamic response.

3.3. Phase-Resolved Transient Evolution of Operational Hydrogen Memory

The endpoint residuals in Figure 3 establish inheritance between exposures, while the phase-resolved analysis in Section 2.7.1 describes how this inherited state develops within each cycle. Figure 4a shows the total releasable content within each cycle. Its phase profile shifts upward over the early cycles and approaches the periodic profile in Figure 4b. Figure 4c separates hydrogen inherited at the start of ON from hydrogen supplied during the current cycle. Both contributions follow the same release rate; their separation records time of entry rather than independently identified fast and slow hydrogen populations.

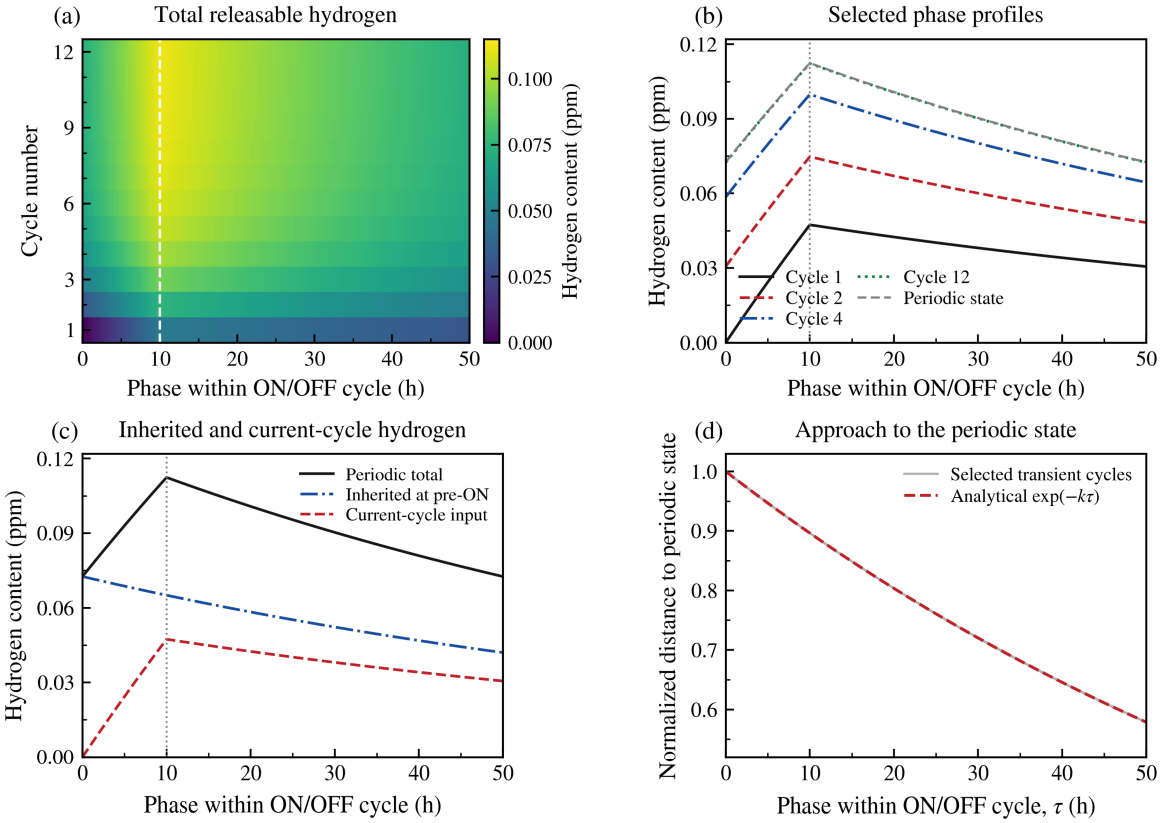


Figure 4. Phase-resolved transient state analysis using the primary single-exponential model: (**a**) releasable hydrogen content as a function of cycle number and phase within the 10 h ON/40 h OFF cycle; (**b**) selected transient phase traces and the periodic state; (**c**) periodic content divided into inherited and current-cycle contributions, both governed by the same release rate; and (**d**) transient-to-periodic gaps normalized by their pre-ON gap. The dashed vertical lines at 10 h in (**a**–**c**) mark input cessation and the start of the OFF period. The contributions in (**c**) are distinguished by time of entry rather than kinetic population.

Figure 4d shows the gap between each transient phase profile and the periodic state, normalized by the gap at the start of ON. The selected traces collapse onto $\exp(-k\tau)$, where τ is time within a cycle, because the transient and periodic responses have the same input. The cycle-to-cycle gap decreases by $\exp[-k(t_{on} + t_{off})]$. The approach to this repeatable phase profile indicates that non-zero releasable hydrogen content remains at the beginning of each new exposure, without indefinite accumulation under the repeated schedule.

3.4. History Dependence Under Equal Cumulative Hydrogen-Input Duration

The equal-exposure schedules defined in Section 2.7.2 are shown in Figure 5a. Each contains 120 h of hydrogen input and 120 h of interruption at the same effective hydrogen input rate; only their segmentation differs.

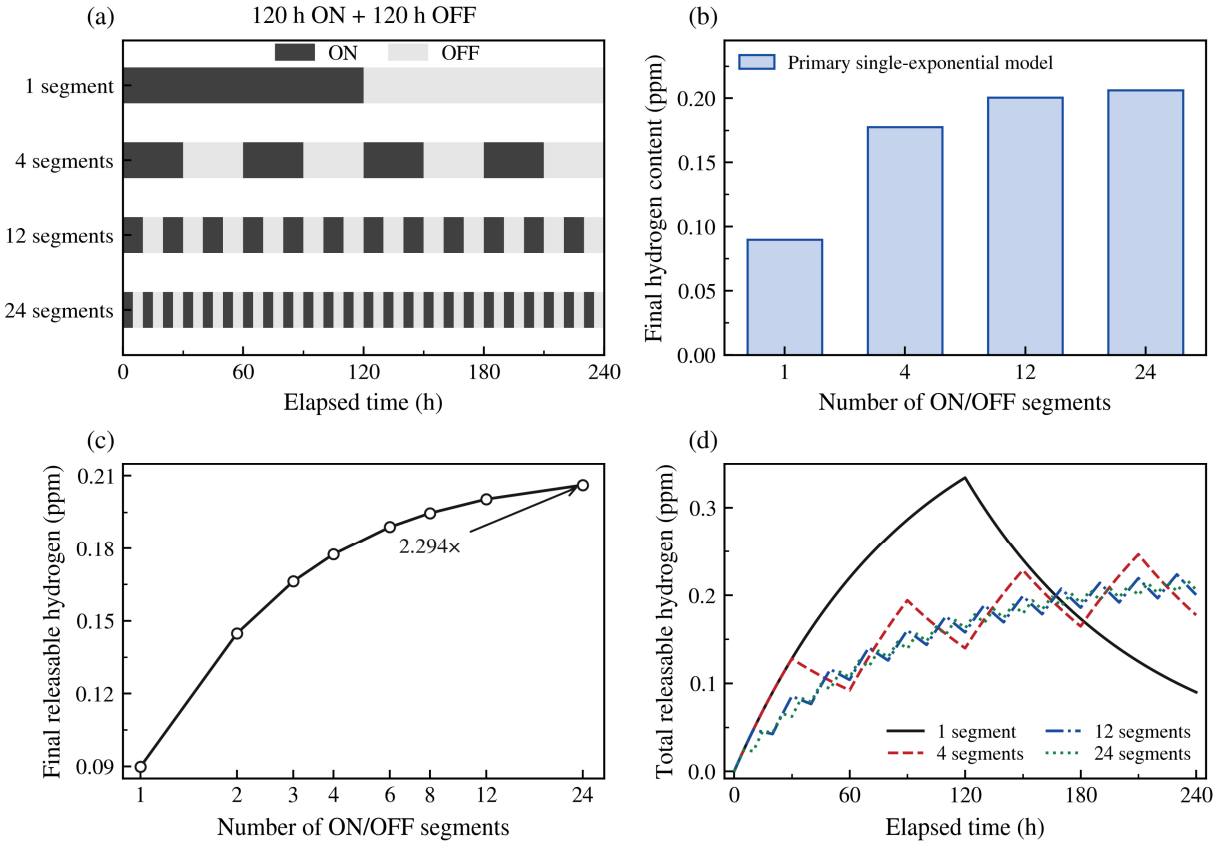


Figure 5. Equal-cumulative-exposure history comparison with 120 h total hydrogen input time and 120 h total interruption time: (**a**) representative ON–OFF schedules; (**b**) final releasable hydrogen contents for selected schedules; (**c**) final releasable hydrogen content versus number of exposure segments; and (**d**) histories of total releasable hydrogen content for representative schedules.

Although the cumulative durations are identical, one long input–interruption pair leaves 0.08989 ppm of releasable hydrogen, while 24 shorter ON–OFF segments leave 0.20618 ppm. Figure 5b–d show that the timing of supply and release accounts for this difference. Short interruptions allow hydrogen to be transferred repeatedly into the next segment before it can fully decay; some input also occurs closer to the final observation. The 24-to-one endpoint ratio is 2.294. Under the present retention kinetics, cumulative hydrogen input duration alone is an incomplete state descriptor, and the temporal arrangement of exposure and interruption supplies an additional operating history variable.

3.5. Operating History Parameter Space Analysis

The parameter space analysis in Section 2.7.3 extends the selected equal-cumulative-exposure comparisons to a range of operating histories. Figure 6a shows the joint influence of the effective hydrogen input rate and interruption duration on the normalized hydrogen memory index. At a fixed interruption duration, increasing the input rate raises the periodic residual because each ON period supplies more releasable hydrogen. At a fixed input rate, a longer interruption allows the releasable hydrogen content to decay further and reduces the inherited state. The duty history map in Figure 6b shows a similar competition between period durations: longer hydrogen input periods raise the periodic state, while longer interruptions reduce the normalized residual.

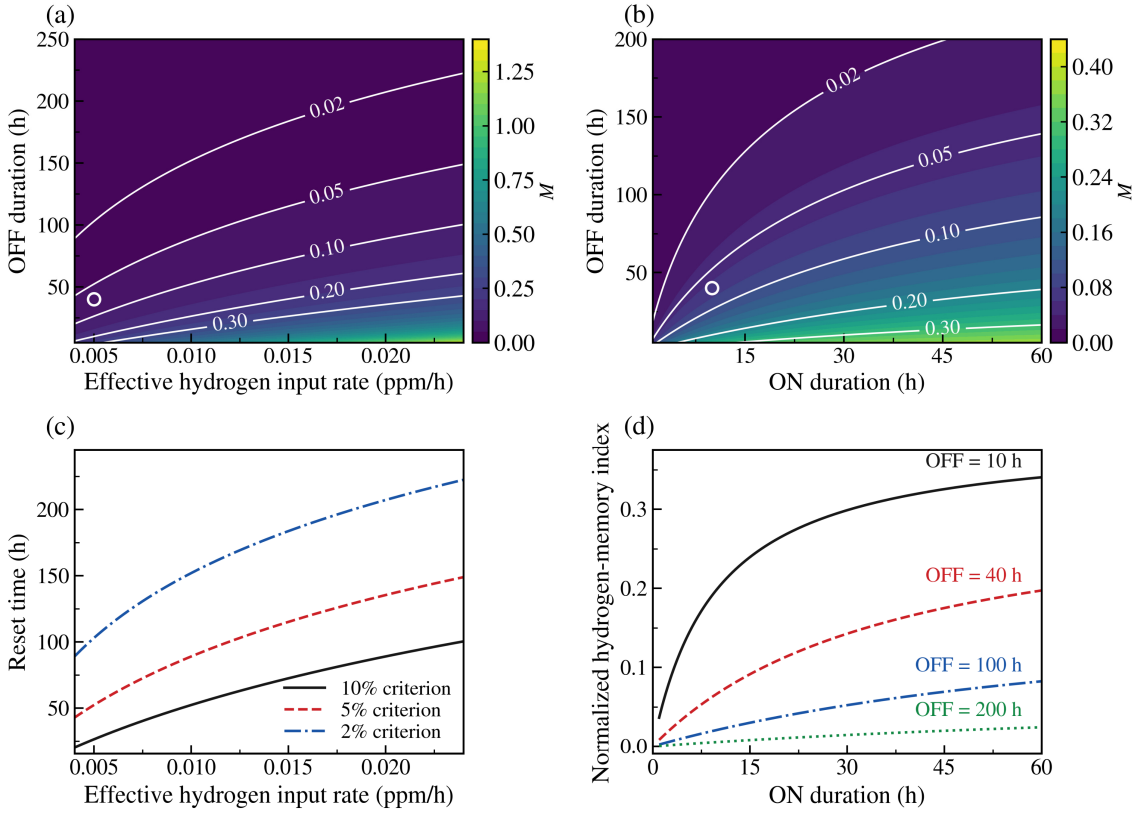


Figure 6. Operating history dependence of the periodic hydrogen state: (**a**) effective hydrogen input rate versus interruption duration; (**b**) hydrogen input duration versus interruption duration at the representative hydrogen input rate; (**c**) minimum periodic OFF duration versus effective hydrogen input rate for 10%, 5%, and 2% normalized residual criteria; and (**d**) hydrogen memory index versus input duration for selected interruption times. Open circles in (**a**,**b**) mark the baseline condition; white contours label normalized residual values. The reference content is C_{ref} = 1.08259 ppm. The residual criteria are schedule comparison measures, not experimentally established damage thresholds.

Figure 6c and Table 5 give the interruption durations required to satisfy the reset criteria. At the representative hydrogen input rate, the 10%, 5%, and 2% normalized residual criteria correspond to approximately 26.33, 52.26, and 102.94 h, respectively. These criteria compare the periodic pre-ON residual with C_{ref} = 1.08259 ppm. They differ from the fraction released during one interruption: an isolated 90% reduction of the starting inventory requires $\ln(10)/k$ = 210.48 h under the same kernel. The response to input duration also varies with interruption duration, as shown in Figure 6d.

Table 5. Minimum periodic OFF durations at 10 h ON, calculated with the primary single-exponential model and C_{ref} = 1.08259 ppm.

Effective Hydrogen Input Rate	Source Basis	10% Criterion	5% Criterion	2% Criterion
0.0040666 ppm/h	30 h HCA conditional benchmark [18]	20.56 h	43.42 h	89.96 h
0.00500 ppm/h	Baseline	26.33 h	52.26 h	102.94 h
0.0062172 ppm/h	30 h broader HCA category [18]	33.35 h	62.64 h	117.50 h
0.02326 ppm/h	Upper rolling-element source scale [17]	98.31 h	146.50 h	219.78 h

3.6. Conditional Uncertainty and Source-Scale Sensitivity

Section 2.7.4 examines uncertainty using 500 joint parametric bootstrap refits of the primary single-exponential model. Figure 7a,b show the coupled fitted parameters and the source amplitudes re-inverted from the unchanged 30 h FE8 mean. The conditional 2.5th–97.5th percentile release rate range is 0.00650–0.01740 h^{-1}. At fixed q = 0.005 ppm/h, the periodic residual spans 0.03937–0.13461 ppm, and the 10% normalized reset spans 13.38–47.19 h. Re-inverting q for each fitted kernel gives 0.00382–0.00445 ppm/h, a periodic residual of 0.03504–0.10272 ppm and a reset of 11.35–35.75 h. These reset percentiles use each refitted amplitude as its own normalized reference.

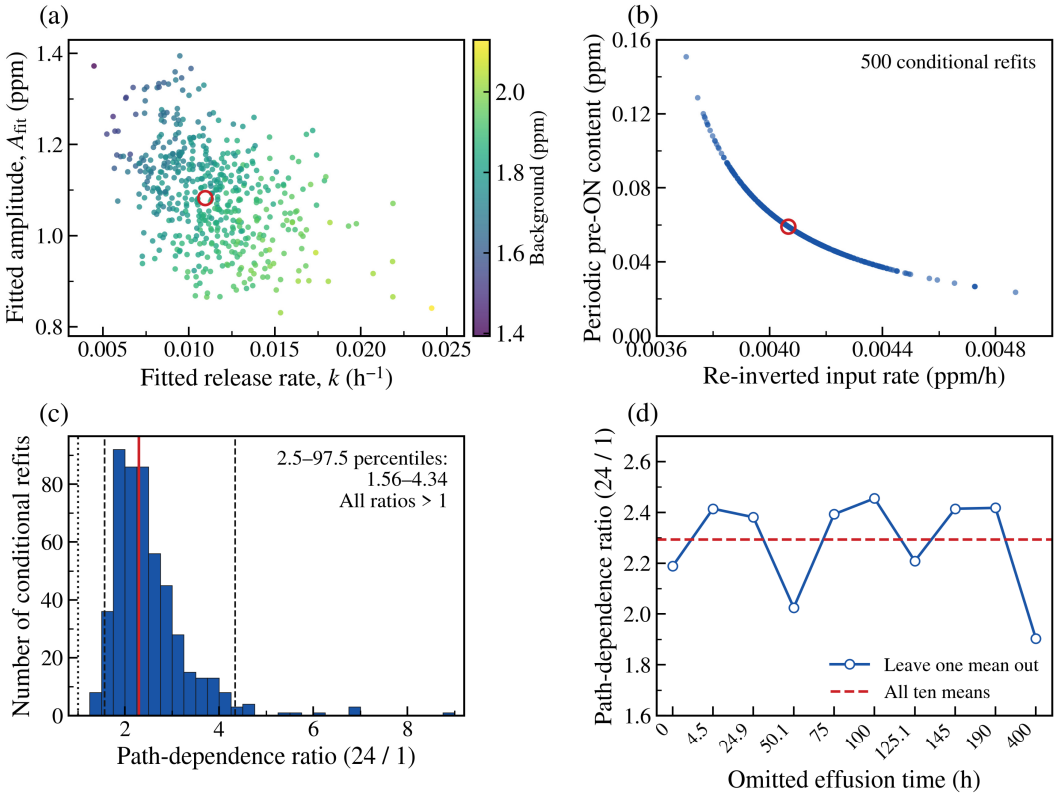


Figure 7. Conditional uncertainty propagation for the primary model: (**a**) joint fitted release rate and amplitude from 500 parametric bootstrap refits, colored by background; (**b**) source amplitudes re-inverted from the 30 h FE8 mean and the corresponding periodic residuals; (**c**) distribution of the 24-to-one endpoint ratio, with dashed lines marking its 2.5th and 97.5th percentiles; and (**d**) the ratio after leaving each effusion mean out in turn. Red reference lines and open circles identify the fit to all ten means. Simulated data use independent additive Gaussian residuals with a fitted scale of 0.10317 ppm. The resulting conditional percentiles are not experimental confidence intervals or bounds on temperature transfer.

Figure 7c,d show that the 24-to-one endpoint ratio remains above one in all 500 refits, with a conditional percentile range of 1.564–4.339; 10 leave-one-out fits give 1.903–2.455. Exposure segmentation therefore changes the final inventory across these refitted kernels, although the magnitude and reset duration remain sensitive to the sparse release data. These are conditional model-based ranges under the assumed residual law rather than experimental measurement confidence intervals.

Propagating the displayed FE8 extents separately gives net increase envelopes of 0.073–0.135 ppm at 30 h and 0.100–0.214 ppm at 50 h. With the primary kernel fixed, their equivalent-source envelopes are 0.00285–0.00528 and 0.00260–0.00556 ppm/h, respectively. These deterministic envelopes retain a shared reference measurement and are distinct from

the release-fit bootstrap. The close agreement of the 30 h and 50 h mean source estimates is therefore not an external validation of the release kernel.

3.7. Model Form and Release Rate Robustness

Figure 8a,b show the fast-rate profile and nominal AICc comparison. The broad profile plateau leaves the additional fast constant unresolved, while the single-exponential fit has the lower AICc. The two-timescale bootstrap also shows substantial instability: 46.5% of the 200 fitted Jacobians are rank deficient, 23.5% of fits place an amplitude at its bound, and 12% reach the numerical upper rate bound. These overlapping diagnostics support use of one primary release scale.

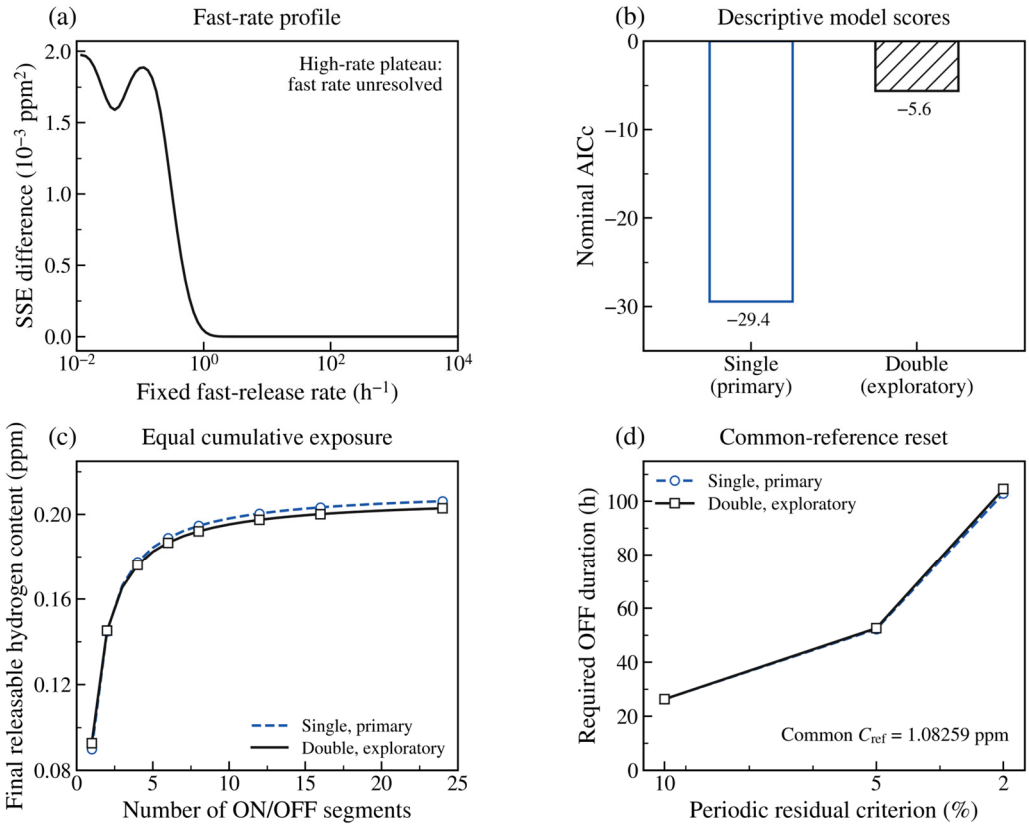


Figure 8. Exploratory model form comparison: (**a**) two-timescale profile SSE difference from its minimum as the fast rate is fixed and the remaining parameters are re-optimized; (**b**) nominal AICc scores with n = 10 and parameter counts of four and six, including residual variance; (**c**) equal-cumulative-exposure final states at the same input rate of 0.005 ppm/h; and (**d**) periodic reset durations using the common primary reference content C_{ref} = 1.08259 ppm. The primary model is single exponential. The two-timescale form is exploratory; its nominal AICc is descriptive because the unresolved component violates regular mixture-model assumptions.

The operating history outputs obtained with the two model forms are compared in Figure 8c,d. The primary single-exponential model gives a baseline normalized memory index of 0.0670 and a 10% reset time of 26.33 h. The exploratory two-timescale refit gives a periodic residual of 0.07288 ppm, close to the primary value of 0.07257 ppm; using the common primary reference amplitude, its 10% reset time is 26.34 h. The final hydrogen content trends under equal cumulative exposure also remain close from one to 24 segments. The corresponding 24-to-one-segment ratios are approximately 2.294 for the single-exponential model and 2.188 for the two-timescale model. The exposure sequence changes the final releasable hydrogen state in both cases, indicating that this conclusion

does not depend on statistically resolving two separate release rate constants from the available effusion data.

In the supplementary deterministic sensitivity sweep, varying the primary release rate by ±20% at a fixed input and reference amplitude gives a normalized memory index of 0.0532–0.0879, a 10% reset duration of 20.56–35.00 h, and a 24-to-one endpoint ratio of 1.887–2.821. Slower release raises the periodic residual and required reset duration. The endpoint ratio instead increases with faster release because the one-pair history has a longer final release interval.

4. Discussion

4.1. Hydrogen Retention and Contact Histories in Bearings

Operational hydrogen memory in Figures 3 and 4 arises from incomplete release between successive periods of input, consistent with established trapping and release behavior [20–27,33,34]. During the first 40 h interruption, Equation (11) gives a 35.4% decrease in releasable hydrogen, from 0.04736 to 0.03058 ppm for the primary model. The retained fraction supplies the initial condition for the next period of input even though substantial hydrogen is released during OFF.

The corresponding hydrogen input history depends on contact chemistry, as well as mechanical loading. Richardson et al. [17] discussed how the interval between contact load cycles may affect oxide film regeneration and hydrogen entry at nascent steel surfaces. Contact recurrence thus connects bearing geometry and operating conditions with surface film recovery and hydrogen supply. Together with the material retention response, these processes determine how much hydrogen can be carried from one loading period into the next.

4.2. Exposure Sequence and Operating Schedules

Figure 5 shows why the exposure sequence must be considered when comparing bearing duty cycles with the same cumulative input and interruption durations. Segmentation changes the time available for each increment of hydrogen to be released before the final measurement, even when the total modeled input is unchanged. Accumulated running hours and the mean duty factor alone therefore cannot specify the final residual.

Periodic steady-state behavior provides a complementary measure of the same process. Integrating Equations (8) and (9) over a complete repeating cycle balances the mean input against the mean release for each component. At a fixed mean effective input, release rate constants and source partition, changing the frequency leaves cycle-averaged releasable content unchanged, while altering the peaks, troughs and their timing. In a bearing, changes in surface film recovery can also alter the effective input [17]. Separating this source change from temporal segmentation allows their contributions to the hydrogen state to be evaluated.

The peak content and final residual also rank schedules differently. The one-segment history in Figure 5d reaches a higher transient maximum and leaves a smaller final residual than the more segmented histories. A design comparison should therefore identify the loading phases at which hydrogen content matters, such as renewed contact after an interruption or a period of high load. This relates the computed hydrogen history to the mechanical history that the bearing actually experiences.

The model form, conditional bootstrap and leave-one-out comparisons support the consistency of this segmentation effect (Figure 8 and Supplementary Materials). Table 6 places the modeled hydrogen contents alongside published bearing-hydrogen measurements and their experimental contexts.

Table 6. Quantitative bearing-hydrogen benchmarks used to contextualize the present model.

Study	Condition	Published Quantitative Observation	Relation to Present Work
Ciruna and Szieleit [1]	Hydrogen-impregnated AISI 52100/440C RCF	RCF life decreased as hydrogen content increased	Historical damage context only
Vegter and Slycke [3]	Hydrogen-charged bearing steel	Approx. 5 wppm strongly promoted spalling/WEC	High-H damage context; not a reset threshold
Paladugu et al. [16]	WEC-critical additive oil vs. mineral oil	Critical oil bearing life below 5% of mineral oil life	Demonstrates lubricant-dependent operating history
Liang et al. [7]	NaCl-electrolyte-precharged bearing steel, 1.6×10^7 RCF cycles	Approx. 3× void density and 4× crack-length density vs. H-free condition	Microdamage context
Weniger et al. [6]	Thiourea/NaOH-precharged 100Cr6 rolling/sliding	Approx. 1.4–2 wppm diffusible H associated with roughly doubled damage-area fraction	Low-wppm damage benchmark; different H metric
Linzmayer et al. [18]	FE8 100Cr6 washers; HCA at 210 °C for 24 h	Freely movable H: 0.055 ± 0.003 ppm reference, 0.159 ± 0.028 ppm at 30 h and 0.212 ± 0.054 ppm at 50 h; reported within/between-washer scatter	Conditional effective input rate benchmark and source-scale consistency check
Richardson et al. [17]	FE8 100Cr6 rolling elements; ramped TDA–GC (setup 2)	Hydrogen increased with duration; approx. 0.40→0.78 ppm at 18 h in the comparison used here	Upper input rate sensitivity envelope
Baur et al. [29]	Gas-charged 100Cr6, room-temperature effusion	Approx. 3 ppm after charging and approx. 1.8 ppm after 400 h	Primary hydrogen retention dataset
Present single-exponential model	Baseline 0.005 ppm/h, 10 h ON/40 h OFF; equal-cumulative-exposure schedules	0.0306 ppm after cycle 1; 0.0725 ppm after cycle 12; 0.0726 ppm periodic residual. With 120 h total ON and 120 h total OFF, final releasable hydrogen content changes from 0.0899 to 0.2062 ppm as the number of segments increases from 1 to 24.	Predicted history-dependent releasable hydrogen content; model output, not a damage threshold

4.3. Matching Bearing Design to Hydrogen Input and Release

The ON–OFF analysis provides a basis for screening bearing hydrogen histories by matching measured uptake and release responses to operating conditions. Figures 6–8 identify the effective input, interruption duration and material retention as coupled contributors to the hydrogen state before renewed loading. For fixed release parameters, source partitions and interval durations, Equation (12) makes the periodic residual proportional to the effective hydrogen input rate. Longer OFF intervals lower that residual. The design opportunity is therefore to consider how geometry and operation influence both entry and the available release interval, alongside load capacity and lubrication performance. Figure 9 relates the calculated hydrogen histories to the bearing variables and release processes used in the proposed design assessment.

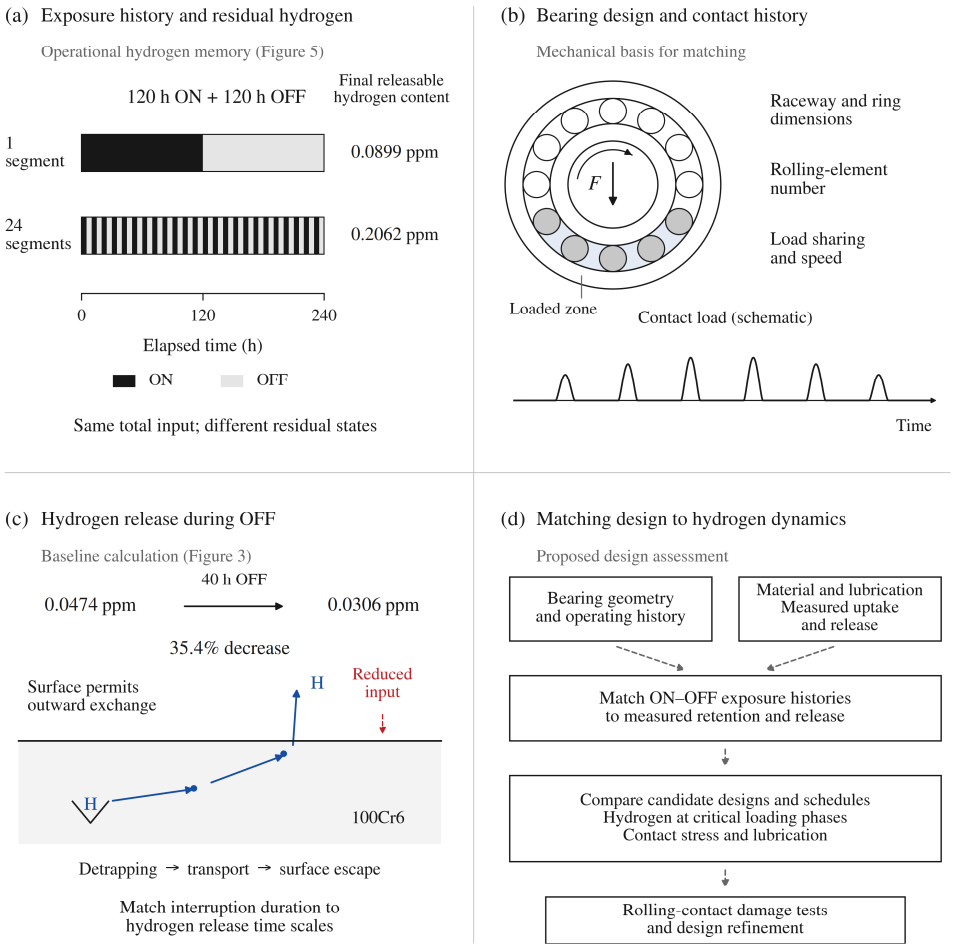


Figure 9. Exposure history effects and a proposed assessment of bearing hydrogen histories: (**a**) final releasable hydrogen contents from the equal-exposure calculations in Figure 5, with identical initial conditions and effective input rate, and 120 h total ON and 120 h total OFF; (**b**) bearing geometry and operating variables with a schematic contact load history; (**c**) releasable hydrogen content before and after the first 40 h OFF interval of the baseline 10 h ON/40 h OFF cycle at 0.005 ppm/h, together with a schematic escape pathway; (**d**) proposed matching of exposure histories to measured uptake and release, followed by comparison of candidate designs and damage test validation.

Figure 9a summarizes the exposure history effect, while Figure 9b identifies the bearing variables through which the loading sequence can be changed. Contact analysis would supply the pressure and sliding histories for a selected geometry and operating condition; hydrogen uptake measurements under the corresponding surface and lubrication conditions would then constrain the effective input history.

Experimental evidence gives a material-level reason to examine release-promoting intervals. Baur et al. [29] reported that gas-charged 100Cr6 specimens stored in ambient air for 400 h recovered tensile strength and ductility to values close to those of the uncharged reference. They attributed this recovery to the effusion of mobile hydrogen. This observation motivates using low-input intervals to reduce retained hydrogen before subsequent service loading.

Figure 9c connects the baseline OFF reduction with the physical processes needed for hydrogen to leave the steel. The schematic path below the numerical comparison represents detrapping, transport toward the surface and surface escape. Net release occurs when the outward transport exceeds the continuing entry and the surface permits hydrogen to escape. The useful duration of an interval therefore depends on the depth of the retained hydrogen and its transport to an escape surface. Longer standby periods under low external supply

provide one possible opportunity; temperature control during such intervals is another variable for experimental assessment.

Material and surface selection enter the same matching problem through their effects on uptake and retention. Weniger et al. [30] observed changes in trapping behavior after mild rolling/sliding tribotesting and noted that less deeply trapped hydrogen may become more mobile. Removal then involves transport of this mobile hydrogen to an escape surface. The conditional uncertainty in Figure 7 also shows why measured retention responses after heat treatment or surface modification are needed before comparison with the intended contact and operating intervals.

Figure 6c and Table 5 give a quantitative reference for comparing interruption durations in repeating schedules using Equation (15). The primary model times for residuals of 10%, 5% and 2% of the fitted initial releasable amount are 26.3, 52.3 and 102.9 h, respectively. For a single maintenance or standby interval with negligible input, Equation (11) instead starts from the hydrogen state inherited from the preceding service history. Removing 90% of an isolated initial inventory takes 210.5 h with the fitted primary release rate; this differs from the periodic criterion in Equation (15).

Figure 9d sets out a proposed sequence for comparing candidate geometries and operating schedules. The calculation would use measured uptake and release responses for the selected material and lubrication conditions. Each candidate is then evaluated through the predicted hydrogen history, including transient peaks and the residual before renewed loading. Comparison at mechanically relevant phases relates these hydrogen measures to contact stress and lubrication performance. Rolling-contact damage tests would assess the selected candidates and guide subsequent design refinement.

4.4. Limitations and Future Work

Quantitative transfer to a particular bearing is limited by the underlying data. The parameterization combines room-temperature effusion of gas-charged 100Cr6 with FE8 tribological uptake measurements [17,18,29]. The 50 h comparison checks conditional source-scale consistency within that FE8 series. The room-temperature release data and 100 °C FE8 accumulation measurements do not form a temperature-consistent calibration; transfer across components, temperatures and lubrication conditions needs further measurements. The effective hydrogen input rate is an inverse model parameter, not a measured interfacial generation flux. The sparse total-effusion data do not uniquely resolve two release timescales; some multistart solutions place the fast decay below the first 4.5 h post-charge sampling interval. The single exponential was therefore adopted for primary predictions. The fast/slow decomposition and amplitude-based source partition are retained only for exploratory sensitivity rather than as identified microscopic trap populations or local detrapping constants. Conditional bootstrap refits quantify the assumed fitting error model; they do not supply experimental confidence intervals or a distribution of digitization error.

The independent 90 °C comparison [37] uses the release rate from a charged, uncracked 52100 plate rather than retained inventory in a bearing. Similar predictions at the withheld points support a parsimonious description within that dataset (Supplementary Materials); they do not calibrate a temperature transfer. The load- and hydrogen-dependent wear observations of Balitskii et al. [38] provide complementary tribological context in different steels, while a quantitative damage criterion still requires the relevant material and loading conditions.

The spatially lumped model describes sustained effective supply and interruption on the hour scale. It excludes contact stress fields, spatial redistribution and damage evolution. Hydrostatic stress gradients, deformation and evolving traps can redistribute

hydrogen during rolling contact [27,39,40], so local hydrogen at a damage site may differ from the computed releasable content. Individual rolling-element passages and loaded-zone transitions are not resolved. A mechanically unloaded interval or shaft stop qualifies as OFF only when the effective hydrogen input becomes negligible; an active environmental entry route can maintain supply.

Short contact gaps require a separate assessment of local transport. Applying the primary fitted half-life of 63.4 h to millisecond intervals gives negligible loss from the lumped inventory. Kürten et al. [41] measured an effective hydrogen diffusivity of 4.9×10^{-12} m^2/s in hardened 100Cr6 at 30 °C. Dividing the square of the distance to an escape surface by this diffusivity gives characteristic times of approximately 0.2 s, 20 s and 34 min for distances of 1, 10 and 100 µm, respectively. Over 1–10 ms, the corresponding diffusion length, $\sqrt{Dt}$, is only 0.070–0.221 µm. These estimates illustrate the role of depth; they are not measured release times or a calibration of the present release response. Repeated passages, local trapping, stress-driven redistribution and surface exchange require spatial analysis when assessing contact-scale transport and escape.

Compared with the McNabb–Foster and Oriani descriptions [20,21,24], the present model replaces spatial diffusion and explicit trap occupancy with a fitted aggregate release response. Its closed-form updates avoid solving a spatial field for each ON–OFF interval, making repeated schedule comparisons straightforward. Finite element transport analyses can instead resolve geometry, concentration and hydrostatic stress gradients and local hydrogen histories [27,39,40]. The present calculations establish neither a measured speed advantage nor higher prediction accuracy relative to those methods. Their contribution is the analytical comparison of inherited inventory under different exposure sequences.

The calculated contents and reset criteria are not validated hydrogen damage thresholds or universal waiting times for safe restarting. The benchmarks in Table 6 use different hydrogen metrics and damage conditions, and tensile recovery after storage does not establish rolling-contact fatigue recovery. Likewise, changing an assumed fast component fraction in the exploratory model does not establish improved damage resistance. Temperature-assisted release would require characterization of the material condition, lubricant behavior and subsequent uptake; the room-temperature rates specify no treatment temperature. The proposed design benefit therefore remains to be assessed in damage tests.

A first validation could compare identical 100Cr6 specimens or bearings with the same total input and interruption times divided into different schedules, as in Figure 5. Load, rolling/sliding conditions, lubricant supply and temperature should be matched during ON, with friction and lubrication transients recorded at restart. Hydrogen measurements at corresponding cycle phases, especially before renewed loading, should use the same component and analysis protocol. Controlling storage and the delay before analysis would account for hydrogen loss during handling [17]. Uptake and release measurements should distinguish net escape from internal redistribution and transfer between trapped and mobile states.

Coupling these measurements with contact and hydrogen transport analyses would relate geometry and speed to local exposure histories. Rolling-contact damage tests could then determine how changes in hydrogen at critical loading phases affect damage initiation and development. This sequence would provide the evidence needed to formulate design criteria for matching bearing structure and operation to hydrogen retention and release.

5. Conclusions

This study used an analytical ON–OFF model constrained by published room-temperature effusion and FE8 accumulation measurements to examine operational hydrogen memory in 100Cr6 bearing steel. The effective input inferred from the 30 h FE8

measurement reproduced the 50 h increment without refitting, with an error below 0.3%, providing a conditional source-scale consistency check. The model relates exposure timing to the hydrogen inherited by subsequent loading. The following conclusions can be obtained:

1. Repeated intermittent exposure approaches a periodic response through the balance between hydrogen input and release. At an effective hydrogen input rate of 0.005 ppm/h with 10 h of input and 40 h of interruption, the first OFF period removed 35.4% of the releasable hydrogen present when input ceased. The post-interruption residual increased from 0.0306 ppm after the first cycle to 0.0725 ppm after 12 cycles, approaching the periodic value of 0.0726 ppm.
2. The exposure sequence determines final releasable hydrogen content alongside cumulative input and interruption durations. With both cumulative durations fixed at 120 h, dividing the schedule into 24 ON–OFF segments instead of one increased the final content from 0.0899 to 0.2062 ppm. The one-segment schedule also reaches a higher transient peak. The peak content and post-interruption residual therefore provide complementary measures for comparing bearing operating histories.
3. The effective hydrogen input rate, input duration, interruption duration and apparent release rate jointly determine the retained content and reset time. In the primary model, periodic residual criteria of 10%, 5% and 2% of the fitted initial releasable amount require OFF intervals of 26.3, 52.3 and 102.9 h, respectively, at 0.005 ppm/h and 10 h ON. Longer OFF intervals or higher apparent release rate constants reduce the residual for otherwise fixed conditions.
4. History dependence persisted in conditional bootstrap refits, leave-one-out calculations and the exploratory two-exponential comparison. The consistent segmentation effect supports including the exposure sequence in bearing hydrogen assessment. Candidate designs can therefore be screened through effective entry, sustained low-input intervals and measured release behavior before contact analysis and damage tests establish their performance at critical loading phases.

Supplementary Materials: The following supporting information can be downloaded at: https://www.mdpi.com/article/10.3390/lubricants14100398/s1, The supplementary archive contains the supporting data, numerical results, Python code, README.md, and Figure S1. Figure S1. Separate approximation of the 90 °C uncracked-specimen release-rate curve: (a) graphical readings and independently fitted single- and double-exponential forms; (b) approximation residuals.

Author Contributions: Conceptualization, H.L.; methodology, H.L.; software, W.L.; validation, B.L.; formal analysis, S.Y. and Z.W.; investigation, S.Y.; resources, W.Z.; data curation, W.L.; writing—original draft preparation, H.L., S.Y. and Z.W.; writing—review and editing, J.F. and B.L.; visualization, W.L.; supervision, W.Z.; project administration, J.F. All authors have read and agreed to the published version of the manuscript.

Funding: This research was funded by the Technological Project of Heilongjiang Province (the Open Competition Mechanism to Select the Best Candidates), China (Grant No. 2023ZXJ04A02); the National Natural Science Foundation of China (Grant No. 52105143); Guangdong Basic and Applied Basic Research Foundation, China (Grant No. 2024A1515010684); Guangdong Basic and Applied Basic Research Foundation, China (Grant No. 2023A1515240059); and the Zhongyuan Support Program for Top Young Talents in Scientific and Technological Innovation of Henan Province.

Data Availability Statement: The digitized literature data, numerical results and calculation code used in this study are available in the Supplementary Materials.

Conflicts of Interest: Author He Liu was employed by the company Luoyang Bearing Research Institute Co., Ltd., and author Jingwen Fang is employed by the company Luoyang Bearing Group

Co., Ltd. The remaining authors declare that the research was conducted in the absence of any commercial or financial relationships that could be construed as a potential conflict of interest.

References

1. Ciruna, J.A.; Szieleit, H.J. The Effect of Hydrogen on the Rolling Contact Fatigue Life of AISI 52100 and 440C Steel Balls. *Wear* **1973**, *24*, 107–118. [CrossRef]
2. Kino, N.; Otani, K. The Influence of Hydrogen on Rolling Contact Fatigue Life and Its Improvement. *JSAE Rev.* **2003**, *24*, 289–294. [CrossRef]
3. Vegter, R.H.; Slycke, J.T. The Role of Hydrogen on Rolling Contact Fatigue Response of Rolling Element Bearings. *J. ASTM Int.* **2010**, *7*, 1–12. [CrossRef]
4. Evans, M.-H.; Richardson, A.D.; Wang, L.; Wood, R.J.K. Effect of Hydrogen on Butterfly and White Etching Crack (WEC) Formation under Rolling Contact Fatigue (RCF). *Wear* **2013**, *306*, 226–241. [CrossRef]
5. Oezel, M.; Schwedt, A.; Janitzky, T.; Kelley, R.; Bouchet-Marquis, C.; Pullan, L.; Broeckmann, C.; Mayer, J. Formation of White Etching Areas in SAE 52100 Bearing Steel under Rolling Contact Fatigue—Influence of Diffusible Hydrogen. *Wear* **2018**, *414–415*, 352–365. [CrossRef]
6. Weniger, L.-M.; Jamil, K.; Sefer, B.; Pelcastre, L.; Åkerfeldt, P.; Olsson, C.-O.A.; Hardell, J. Quantifying Hydrogen Concentrations and Their Influence on Surface-Initiated Damage in Rolling/Sliding Contacts of 100Cr6 Bearing Steel. *Tribol. Lett.* **2025**, *73*, 73. [CrossRef]
7. Liang, X.Z.; Zhao, G.-H.; Owens, J.; Gong, P.; Rainforth, W.M.; Rivera-Díaz-del-Castillo, P.E.J. Hydrogen-Assisted Microcrack Formation in Bearing Steels under Rolling Contact Fatigue. *Int. J. Fatigue* **2020**, *134*, 105485. [CrossRef]
8. Ruellan, A.; Ville, F.; Kleber, X.; Arnaudon, A.; Girodin, D. Understanding White Etching Cracks in Rolling Element Bearings: The Effect of Hydrogen Charging on the Formation Mechanisms. *Proc. Inst. Mech. Eng. Part J J. Eng. Tribol.* **2014**, *228*, 1252–1265. [CrossRef]
9. Richardson, A.D.; Evans, M.-H.; Wang, L.; Wood, R.J.K.; Ingram, M.; Meuth, B. The Evolution of White Etching Cracks (WECs) in Rolling Contact Fatigue-Tested 100Cr6 Steel. *Tribol. Lett.* **2018**, *66*, 6. [CrossRef] [PubMed]
10. Evans, M.-H.; Wang, L.; Wood, R.J.K. Formation Mechanisms of White Etching Cracks and White Etching Area under Rolling Contact Fatigue. *Proc. Inst. Mech. Eng. Part J J. Eng. Tribol.* **2014**, *228*, 1047–1062. [CrossRef]
11. Evans, M.-H. An Updated Review: White Etching Cracks (WECs) and Axial Cracks in Wind Turbine Gearbox Bearings. *Mater. Sci. Technol.* **2016**, *32*, 1133–1169. [CrossRef]
12. López-Uruñuela, F.J.; Fernández-Díaz, B.; Pagano, F.; López-Ortega, A.; Pinedo, B.; Bayón, R.; Aguirrebeitia, J. Broad Review of "White Etching Crack" Failure in Wind Turbine Gearbox Bearings: Main Factors and Experimental Investigations. *Int. J. Fatigue* **2021**, *145*, 106091. [CrossRef]
13. Kürten, D.; Khader, I.; Kailer, A. Tribochemical Degradation of Vacuum-Stable Lubricants: A Comparative Study between Multialkylated Cyclopentane and Perfluoropolyether in Vacuum Ball-on-Disc and Full-Bearing Tests. *Lubr. Sci.* **2020**, *32*, 183–191. [CrossRef]
14. Kürten, D.; Winzer, N.; Kailer, A.; Pfeiffer, W.; Spallek, R.; Scherge, M. In-Situ Detection of Hydrogen Evolution in a Lubricated Sliding Pin-on-Disk Test under High Vacuum. *Tribol. Int.* **2016**, *93*, 324–331. [CrossRef]
15. Kürten, D.; Khader, I.; Raga, R.; Casajús, P.; Winzer, N.; Kailer, A.; Spallek, R.; Scherge, M. Hydrogen Assisted Rolling Contact Fatigue due to Lubricant Degradation and Formation of White Etching Areas. *Eng. Fail. Anal.* **2019**, *99*, 330–342. [CrossRef]
16. Paladugu, M.; Lucas, D.R.; Hyde, R.S. Effect of Lubricants on Bearing Damage in Rolling-Sliding Conditions: Evolution of White Etching Cracks. *Wear* **2018**, *398–399*, 165–177. [CrossRef]
17. Richardson, A.D.; Evans, M.H.; Wang, L.; Wood, R.J.K.; Ingram, M. Thermal Desorption Analysis of Hydrogen in Non-hydrogen-Charged Rolling Contact Fatigue-Tested 100Cr6 Steel. *Tribol. Lett.* **2018**, *66*, 4. [CrossRef] [PubMed]
18. Linzmayer, M.; Gutiérrez Guzmán, F.; Manke, G.; Jacobs, G.; Sous, C.; Pohl, M. Post-Testing Measurement of Freely Movable and Diffusible Hydrogen in Context of WEC Formation at Cylindrical Roller Thrust Bearings from 100Cr6. *Friction* **2021**, *9*, 876–890. [CrossRef]
19. Wranik, J.; Holweger, W.; Wang, L. The Influence of Peripheral Components in Test Rig Creation of White Etching Cracks. *Lubricants* **2024**, *12*, 45. [CrossRef]
20. McNabb, A.; Foster, P.K. A New Analysis of the Diffusion of Hydrogen in Iron and Ferritic Steels. *Trans. Metall. Soc. AIME* **1963**, *227*, 618–627. Available online: https://aimehq.org/themes/custom/aime/doclibrary/transactions/vol227.html (accessed on 14 October 2026).
21. Oriani, R.A. The Diffusion and Trapping of Hydrogen in Steel. *Acta Metall.* **1970**, *18*, 147–157. [CrossRef]
22. Pressouyre, G.M. A Classification of Hydrogen Traps in Steel. *Metall. Trans. A* **1979**, *10*, 1571–1573. [CrossRef]
23. Pressouyre, G.M. Trap Theory of Hydrogen Embrittlement. *Acta Metall.* **1980**, *28*, 895–911. [CrossRef]
24. Krom, A.H.M.; Bakker, A. Hydrogen Trapping Models in Steel. *Metall. Mater. Trans. B* **2000**, *31*, 1475–1482. [CrossRef]

25. Choo, W.Y.; Lee, J.Y. Thermal Analysis of Trapped Hydrogen in Pure Iron. *Metall. Trans. A* **1982**, *13*, 135–140. [CrossRef]
26. Kumnick, A.J.; Johnson, H.H. Deep Trapping States for Hydrogen in Deformed Iron. *Acta Metall.* **1980**, *28*, 33–39. [CrossRef]
27. Benannoune, S.; Charles, Y.; Mougenot, J.; Gaspérini, M. Numerical Simulation of the Transient Hydrogen Trapping Process Using an Analytical Approximation of the McNabb and Foster Equation. *Int. J. Hydrogen Energy* **2018**, *43*, 9083–9093. [CrossRef]
28. Baur, M.; Khader, I.; Kürten, D.; Schieß, T.; Kailer, A.; Dienwiebel, M. Premature Damage in Bearing Steel in Relation with Residual Stresses and Hydrogen Trapping. *Lubricants* **2024**, *12*, 311. [CrossRef]
29. Baur, M.; Khader, I.; Kürten, D.; Reißig, L.; Schweizer, F.; Kailer, A.; Dienwiebel, M. Hydrogen Uptake of 100Cr6 Bearing Steel in Gaseous Pressurized Hydrogen and Resulting Tensile Strength. *J. Iron Steel Res. Int.* **2026**, *33*, 184. [CrossRef]
30. Weniger, L.-M.; Sefer, B.; Pelcastre, L.; Åkerfeldt, P.; Hardell, J. Influence of Lubricated Rolling/Sliding Tribotesting on Hydrogen Trapping in 100Cr6 Bearing Steel. *Tribol. Lett.* **2024**, *72*, 69. [CrossRef]
31. Panda, A.; Davis, L.; Ramkumar, P.; Amirthalingam, M. The Role of Size and Volume Fraction of Carbides on Hydrogen Embrittlement and White Etching Areas Formation in Bearing Steel under Dynamic Loading. *Int. J. Fatigue* **2023**, *176*, 107837. [CrossRef]
32. Panda, A.; Davis, L.; Ramkumar, P.; Amirthalingam, M. The Role of Retained Austenite against Hydrogen Embrittlement and White Etching Area Formation in Bearing Steel under Dynamic Loading. *Int. J. Hydrogen Energy* **2024**, *58*, 1359–1371. [CrossRef]
33. Bai, P.; Zhou, J.; Luo, B.; Zheng, S.; Wang, P.; Tian, Y. Hydrogen Embrittlement of X80 Pipeline Steel in H2S Environment: Effect of Hydrogen Charging Time, Hydrogen-Trapped State and Hydrogen Charging-Releasing-Recharging Cycles. *Int. J. Miner. Metall. Mater.* **2020**, *27*, 63–73. [CrossRef]
34. Malo, M.; Peñalva, I.; Roldán, M.; Urrestizala, M.; Monasterio-Guillot, L.; Hendricks, S.J.; García-González, J.M.; Carella, E. Surface and Microstructural Evolution of EUROFER97-3 during Hydrogen Isotope Permeation Experiments. *Mater. Charact.* **2026**, *239*, 116724. [CrossRef]
35. López-Uruñuela, F.J.; Fernández-Díaz, B.; Pinedo, B.; Aguirrebeitia, J. Early Stages of Subsurface Crack and WEC Formation in 100Cr6 Bearing Steel under RCF and Hydrogen Influence. *Int. J. Fatigue* **2022**, *155*, 106587. [CrossRef]
36. NSK Ltd. *Technical Report*; NSK Ltd.: Tokyo, Japan, 2024. Available online: https://www.nsk.com/content/dam/nsk/common/catalogs/ctrgPdf/bearings/e728.pdf (accessed on 12 September 2026).
37. Solano-Alvarez, W.; Song, E.J.; Han, D.K.; Suh, D.-W.; Bhadeshia, H.K.D.H. Cracks in Martensite Plates as Hydrogen Traps in a Bearing Steel. *Metall. Mater. Trans. A* **2015**, *46*, 665–673. [CrossRef]
38. Balitskii, O.I.; Kolesnikov, V.O.; Ivaskevych, L.M.; Havrylyuk, M.R. The Influence of Specific Features of Load and Hydrogen Charging on Steel Tribotechnical Properties. *Mater. Sci.* **2023**, *58*, 505–512. [CrossRef]
39. Martin, M.L.; Dadfarnia, M.; Nagao, A.; Wang, S.; Sofronis, P. Enumeration of the Hydrogen-Enhanced Localized Plasticity Mechanism for Hydrogen Embrittlement in Structural Materials. *Acta Mater.* **2019**, *165*, 734–750. [CrossRef]
40. Barrera, O.; Bombac, D.; Chen, Y.; Daff, T.D.; Galindo-Nava, E.; Gong, P.; Haley, D.; Horton, R.; Katzarov, I.; Kermode, J.R.; et al. Understanding and Mitigating Hydrogen Embrittlement of Steels: A Review of Experimental, Modelling and Design Progress from Atomistic to Continuum. *J. Mater. Sci.* **2018**, *53*, 6251–6290. [CrossRef] [PubMed]
41. Kürten, D.; Khader, I.; Kailer, A. Determining the Effective Hydrogen Diffusion Coefficient in 100Cr6. *Mater. Corros.* **2020**, *71*, 918–923. [CrossRef]

Disclaimer/Publisher's Note: The statements, opinions and data contained in all publications are solely those of the individual author(s) and contributor(s) and not of MDPI and/or the editor(s). MDPI and/or the editor(s) disclaim responsibility for any injury to people or property resulting from any ideas, methods, instructions or products referred to in the content.